The Effect of Different Force Applications on the Protein-Protein Complex Barnase-Barstar

Jan Neumann and Kay-Eberhard Gottschalk*
Angewandte Physik und Biophysik, Ludwig-Maximilians Universität, Munich, Germany

ABSTRACT Steered molecular dynamics simulations are a tool to examine the energy landscape of protein-protein complexes by applying external forces. Here, we analyze the influence of the velocity and geometry of the probing forces on a protein complex using this tool. With steered molecular dynamics, we probe the stability of the protein-protein complex Barnase-Barstar. The individual proteins are mechanically labile. The Barnase-Barstar binding site is more stable than the folds of the individual proteins. By using different force protocols, we observe a variety of responses of the system to the applied tension.

INTRODUCTION

Forces are regulating factors on protein complexes. Application of forces is important in numerous processes in biological systems like cell adhesion or cellular mobility (1–5). In addition, forces are often used as an experimental tool for studying the energy landscapes of both individual proteins and protein-protein complexes (6–8). The interpretation of these experiments is complex and a thorough description of the influence of different force protocols on the unbinding pathways is critical (9). In particular, force-induced unfolding follows pathways that are different from spontaneous free-solution, chemically-induced, or temperature-induced types of unfolding (10,11).

Technically, the application of forces on the nanoscale can be realized using different experimental techniques like atomic force microscopy (AFM), force pipette, optical tweezers, or simulation methods like steered molecular dynamics (SMD) on the single-molecule level (12–22).

The response of secondary structure elements on different orientations of external stresses leads to a large range of unraveling forces (23–25). In more recent studies, the dependence of the mechanical stability of protein unfolding on the force linkage is demonstrated. On the model system of ubiquitin, it is shown, by experiment and simulation, that different ubiquitin linkages in nature differ in their unfolding forces and unfolding free energy profiles (26–28). The unfolding of fibronectin depends critically on the vector of the applied forces (29). The force response and energy landscape of the fluorescence molecule GFP on different force attachment points has been examined using AFM experiments as well as model simulations (28,30,31). An asymmetric nature of the force response of the titin kinase in a symmetrical setup was shown by Gräter et al., demonstrating the direction dependency of the protein response to force (32), recently supported by AFM measurements (33). In force-clamp simulations, possible relations between forced and chemically induced unfolding pathways have been suggested (34). These studies underline the importance of both the history of force application as well as the direction of the force vector for the observed response.

Applied forces have also been used to estimate binding energies and to analyze protein-protein complexes. Recently, SMD simulations were used to force the cytochrome $c2$ unbinding from the reaction center (35), to unbind an antibody-antigen complex (36) as well as to analyze the protein-protein interaction energies of the TCR-pMHC complex (37).

A general advantage of SMD simulations over the experimental techniques is that the chosen unfolding pathway can be analyzed in atomistic detail. However, due to computational limitations, the used velocities exceed the experimental ones by orders of magnitude. This renders a direct comparison between experiment and simulation complicated. Thus, insight into the atomistic response to different force protocols used is crucial for this comparison. Furthermore, it reveals details of the underlying energy landscape not observable without the explicit control over the experimental parameters offered by the simulation.

In this work, we perform SMD simulations on the protein-protein complex Barnase-Barstar. We use different attachment points and different velocities of the force application to observe the response of the model system. This allows us to gain detailed insight into the effect of differently applied forces on a protein complex analogous to the dependence of mechanical stability of protein unfolding on the force linkage.

Barnase is a bacterial RNase, which is excreted by the bacterium *Bacillus amyloliquefaciens* and is deadly to unprotected cells (38–42). The natural inhibitor Barstar protects the bacterium. Due to the high evolutional pressure, the Barnase-Barstar complex is one of the fastest forming and most stable complexes known (43).

The fast association of the Barnase-Barstar is electrostatically facilitated (44–46). Poisson-Boltzmann calculations predicted a stabilizing electrostatic effect in agreement with

Submitted May 16, 2008, and accepted for publication January 13, 2009.

*Correspondence: kay.gottschalk@physik.uni-muenchen.de

Editor: Helmut Grubmüller.

0006-3495/09/09/1687/13 $2.00

doi: 10.1016/j.bpj.2009.01.052

experimental data (47). Brownian dynamics studies of the Barnase-Barstar complex showed that its association is diffusion-limited and the experimentally measured association rates can be reproduced (39,44,48,49). Recently, the free energy landscape of this association has been analyzed. An optimal association pathway was found involving a region close to the RNA binding loop of the protein complex (50,51). An overlap of association and dissociation pathways, using rigid-body Brownian dynamics simulations with an implicit solvent model, has been suggested (51). Although the equilibrium association of the Barnase-Barstar complex has been studied to a great extent, the response of the complex to nonequilibrium conditions has not been examined as thoroughly. However, during export of the complex, it is exposed to forces. Furthermore, protein complexes are in general an attractive target for force studies: the probing of protein-protein complexes by force can be regarded as a complex differential assay, where the mechanical stability of the individual folds is compared to the stability of the noncovalent binding site, depending on a variety of experimental parameters.

The aim of this study is to investigate the mechanical stability of this model complex under the influence of different force applications. Since Barnase needs to be exported from the cell, we expect a low mechanical stability of the individual protein. However, since the cell needs to be protected as long as Barnase is not exported, we expect a high stability of the Barnase-Barstar binding site inhibiting RNA binding. Indeed, we demonstrate here that the complex binding site is more stable than the individual domains. We recapture basic features of the unbinding transition state. We show that we can alter the main trajectory from unfolding to several unbinding pathways by altering the attachment points of the steering forces. Hence, our simulations probe, in a differential force assay, the relative stability of regions within the complex, depending on the force protocol used.

METHODS

All simulations on the Barnase-Barstar complex (PDB code: 1BRS (52)) were performed with the MD simulation software GROMACS Ver. 3.2–3.3.3 (53,54). Periodic boundary conditions, SPC/E (55) water, and OPLS-AA (56) force field were used for all simulations.

System preparation

The Barnase-Barstar structure was preoriented in a 4 nm × 5.8 nm × 12 nm waterbox. The vector connecting $C_\alpha^{\mathrm{bn}}7$ and $C_\alpha^{\mathrm{bs}}86$ was oriented parallel to the z axis of the box. Thirteen Na^+ and nine Cl^- atoms were added to neutralize the overall charge of the system at a 75 mM NaCl concentration.

Energy minimization was performed with steepest descent and with a maximum step size of 0.01 nm. A cutoff radius of 1 nm for Coulomb and van der Waals interactions was used.

A 200-ps positional restraint simulation followed. All protein atoms were restrained by a harmonic potential with a harmonic force constant of $2000\frac{\mathrm{kJ}}{\mathrm{mol}\cdot\mathrm{nm}^2} = 3.32\frac{\mathrm{nN}}{\mathrm{nm}}$. All bonds were constrained via the LINCS algorithm (57). The COM translation of the system was removed. Berendsen temperature coupling (58) was used to couple the protein atoms and the nonprotein atoms separately in two groups with a temperature bath of 300 K and a time-constant of 0.1 ps.

For all further simulations, electrostatics were calculated with fast particle-mesh Ewald electrostatics (59) with an order of four and a cutoff for Coulomb and van der Waals interactions of 1.0 nm.

Five-hundred picoseconds of equilibration were performed using the leap-frog algorithm with a timestep of 2 fs. All C_α backbone-atoms were restrained with a harmonic potential with a force constant of $200\frac{\mathrm{kJ}}{\mathrm{mol}\cdot\mathrm{nm}}$ to avoid a rotation of the system. For equilibration and all SMD runs, the protein complex and the solvent molecules were coupled to two separate Berendsen thermostats, setting each temperature to 300 K. In addition, Berendsen pressure coupling (58) set the whole system to 1 bar with a compressibility of 4.5×10^{-5} bar^{-1} and a time-constant of 0.5 ps. The final structure of this equilibration step was used as the initial structure for all SMD simulations.

Before an SMD was started, velocities were again randomly assigned and another 200-ps equilibration were performed.

SMD simulation

For all setups, constant velocity pulling simulations with fast ($\upsilon_{\mathrm{fast}} = 2\frac{\mathrm{nm}}{\mathrm{ns}}$), medium ($\upsilon_{\mathrm{medium}} = 0.5\frac{\mathrm{nm}}{\mathrm{ns}}$), and slow ($\upsilon_{\mathrm{slow}} = 0.125\frac{\mathrm{nm}}{\mathrm{ns}}$) pulling velocities was done. The COM movement was removed for the atom/group where the complex was fixed in space. A harmonic potential with a spring constant of $k = 1600\frac{\mathrm{kJ}}{\mathrm{mol}\cdot\mathrm{nm}^2} = 2.66\frac{\mathrm{nN}}{\mathrm{nm}}$ was moved in z direction until the final position was at least 3.5 nm (up to 6 nm) away from the initial position. The majority was pulled 5 nm, which results in a pulling time of 2.5 ns for fast, 10 ns for medium, and 40 ns for slow pulling trajectories. The hard spring constantly forces the atom to closely follow the harmonic potential spatially and in time. Because the spring constant was kept constant, its influence on the loading rate of the AFM did not vary in Setups 1–3. The number of simulated trajectories per setup and pulling velocity can be found in Table 1.

Setup 1

The harmonic potential mimicking an AFM tip was attached to the C_α atom of the first residue of the first element with regular secondary structure of Barnase ($C_\alpha^{\mathrm{bs}}86$) and fixed the position of the C_α atom of the last residue of the last element with regular secondary structure of Barstar ($C_\alpha^{\mathrm{bn}}7$) in Setup 1. For the mirrored setup, Setup 1_{m}, the attachment points for pulling and spatial fixation were exchanged (Fig. 1 *B*).

Setup 2

The COM of Barstar was pulled by the time-dependent harmonic potential, whereas the COM of Barnase was fixed.

Setup 3

For the direct probing of the protein-protein binding site, the COM of the C_α values of the Barstar binding helix was the attachment point of the force. The COM of Barnase was fixed like in Setup 2. Only fast pulling was simulated. Due to the early unbinding of the protein complex, the pulling was only simulated for 2.25 ns, corresponding to a pulling length of 4.5 nm.

Calculation of effective force and work

First, the time of separation for each single trajectory in Setups 2 and 3 was determined. The forces exerted on the system after the separation were assumed to be the drag forces of the molecule through the solvent water. These drag forces were averaged for each trajectory individually from the time of the separation to the end of the simulation. To renormalize the forces after the separation to zero, we subtracted the average drag forces from the calculated forces. This resulted in an effective force F_{eff} for the separation:

$$F_{\mathrm{eff}}(x) = F(x) - \langle F_{\mathrm{drag}} \rangle. \quad (1)$$

TABLE 1 The average maximum forces (unfolding for Setups 1 and 1_m; unbinding for Setups 2 and 3) for the different pulling velocities are given with the standard deviation of the forces as error; $\langle \ldots \rangle$ denotes the average

	Velocity	Attachment	Loading rate/ $\frac{pN}{ns}$	$\langle F_{max} \rangle$/pN	Error/pN	No. of trajectoriespathway/total number per setup
Setup 1, unfolding						
Barnase	Fast	C-C	5320	951	61	12/77
	Medium	C-C	1330	799	55	24/31
	Slow	C-C	332,5	753	61	7/12
Barstar	Fast	C-C	5320	903	82	67/77
	Medium	C-C	1330	809	58	14/31
	Slow	C-C	332,5	762	33	5/12
Setup $1_{m,}$ unfolding						
Barnase	Fast	C-C	5320	827	57	70/73
	Medium	C-C	1330	732	53	15/15
	Slow	C-C	332,5	737	97	12/12
Barstar	Fast	C-C	5320	855		1/73
Setup 2, unbinding						
	Fast	COM-COM	5320	1310	95	9/67
	Medium	COM-COM	1330	1123	65	10/10
	Slow	COM-COM	332,5	938	97	8/8
Setup 3, unbinding						
	Fast	Helix-COM	5320	1702	175	55/55
	Medium	Helix-COM	1330	1332	214	10/10
	Slow	Helix-COM	332,5	1168	201	8/8

The effective work done during the separation of the complex was calculated by

$$W_{\text{eff}}(x) = \sum_{i}^{x_i \le x} F_{\text{eff}}(x_i) \times (x_i - x_{i-1}). \quad (2)$$

These work curves $W_{\text{eff}}(x)$ were then averaged for each pulling velocity of Setups 2 and 3. No average work distributions for Setups 1 and 1_m were calculated since no unbinding is seen.

RESULTS

To understand the influence of force application on the complex, the unfolding pathways need to be described. Due to the high complexity of the system, an approach to reduce this complexity to a small set of descriptive parameters is needed.

We analyzed the unbinding pathways by defining characteristic contacts in the protein, which open during the simulation. A careful analysis of our trajectories led to the definition of the five specific contacts for the description of the unfolding pathways.

The contacts 1 and 3 are within Barstar. The contact 2 is a contact within Barnase, while the contacts 4 and 5 are between both complex partners (Fig. 1, Table 2). The calculation of the average fluctuations of these specific contacts during the whole equilibration show stochastic fluctuations

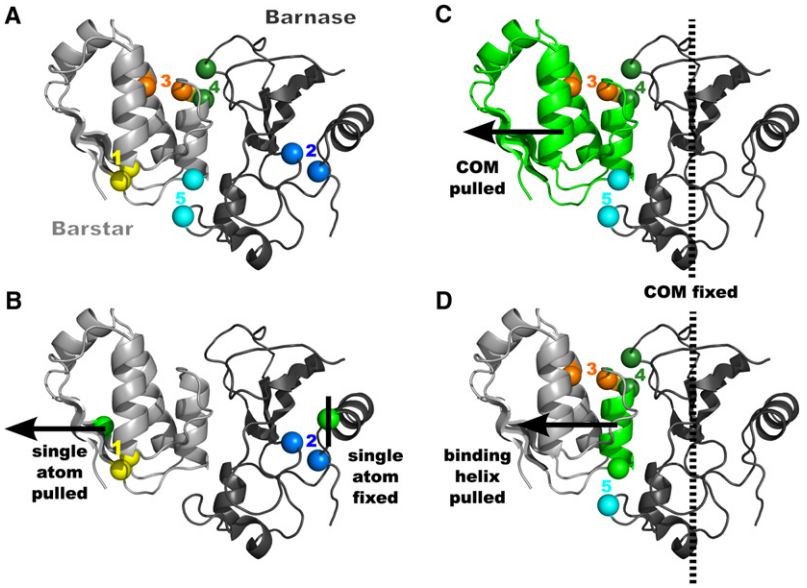

FIGURE 1 (*A*) Contact points for the analysis of the pathways. The molecular structure of Barnase (*dark gray*) complexing Barstar (*light gray*). The specific contacts chosen for a description of the unfolding pathways are shown as colored spheres and denoted with numbers 1–5. (*B*) Setup 1. The moving potential was attached to the last C_α-atom $C_\alpha^{bs}86$ of the last secondary structural element of Barstar (highlighted and with *velocity arrow* in the direction of pulling), while the spatially fixed potential was located at $C_\alpha^{bn}7$ (with *vertical line*), the first C_α-atom of the first secondary structure element of Barnase (*dark gray*). (*C*) Setup 2. The moving potential was attached directly to the COM of Barstar (left molecule), while the spatially fixed potential was attached to the COM of Barnase (right molecule). (*D*) Setup 3. For a direct probing of the binding site, the moving potential was located at the Barstar binding helix (highlighted and with *velicity arrow*), while the static potential was attached to the COM of Barnase (*dark gray*).

TABLE 2 The contact separation distances d_i and the characteristic atoms used in the analysis to determine the trajectory path

Contact	Side chain 2	Side chain 2	d_i^{eq}/nm;in nm	f_i^{eq}/nm;in nm
d_1	$Leu_{bs}49$	$Ile_{bs}84$	0.48	0.02
d_2	$Asn_{bn}5$	$Ile_{bn}76$	0.53	0.02
d_3	$Leu_{bs}34$	$Val_{bs}70$	0.65	0.02
d_4	$Arg_{bn}59$	$Asp_{bs}35$	0.58	0.04
d_5	$Ser_{bn}38$	$Trp_{bs}44$	0.52	0.04

The contacts are given with the three-letter code of the amino acid with the chain at lower position (*bn*, Barnase; *bs*, Barstar) and the number of the residue in the chain. For each specific contact, the average equilibrium distance d_i^{eq} with its average fluctuation f_i^{eq} is given.

of their C_α–C_α distances of <0.05 nm. This indicates that they are in stable regions of the protein complex. However, depending on the setup, these contacts separate at certain times in our simulation. A contact is defined as separated if the specific C_α–C_α distance of the contact is increased by 0.5 nm relative to the starting structure of the simulation (Fig. 2).The pathways are characterized by the pulled distances d_1–d_5, at which these specific contacts separate. If the contact did not separate during the simulation, the respective distance was set to zero. By analyzing the histograms of distances d_1–d_5, the response of the protein complex to force can be described.

Setups 1 and 1_m

In Setups 1 and 1_m, we chose to simulate the experimental, directly-accessible force application of the acting force to single C_α atoms.

We examined the effect of the pulling speed on the unfolding pathways of the probed protein complex. The system was simulated using three different pulling velocities ($v_{fast} = 2\frac{nm}{ns}$, $v_{medium} = 0.5\frac{nm}{ns}$, and $v_{slow} = 0.125\frac{nm}{ns}$). We furthermore tested this setup with two mirrored force vectors: first, the moving potential was acting on Barstar (Setup 1, Fig. 1) and second on Barnase (Setup 1_m).

The pathways chosen in these setups are well described by the distances d_1 and d_2 (Fig. 2). The value d_1 is describing the unfolding of the probed Barstar β-sheet, while d_2 is characterizing the concerted motion of the outermost Barstar α-helix away from the core of the protein complex.

Setup 1

Here, the force is acting on $C_\alpha^{bs}86$, while $C_\alpha^{bn}7$ is fixed (*bs*, Barstar; *bn*, Barnase). Two main unfolding pathways and a mixture of the two main pathways were observed (Fig. 3 *A*, *left*).

The unfolding of the Barstar β-sheet, described by d_1, was the main unfolding pathway at v_{fast}. The characteristic contact broke after a pulled distance of 1.7 nm. However, the concerted movement of the Barnase α-helix shearing away from the core of the protein, described by d_2, was the main event at the slower pulling speeds (v_{medium} and v_{slow}). Here, the contact broke after a pulled distance of ~1.4 nm for the medium and at ~0.9 nm for the slow pulling velocity. The maximum force on the main pathway are slightly lower than for the alternative pathway (Table 1). With decreasing pulling velocity, the maximum forces decrease. The mixed unfolding pathway was represented by unfolding at both ends of the protein complex, each side being unfolded analogous to one of the main pathways.

Setup 1_m

Here, we used the mirrored probing protocol of Setup 1 (pulling $C_\alpha^{bn}7$ and fixing $C_\alpha^{bs}86$).

The Setup 1_m shows only one main unfolding pathway. This unfolding of Barnase from the N-terminus is characterized by a distribution of the unbinding distances d_2^{fast} ~1.3 nm, d_2^{medium} ~1.0 nm, and d_2^{slow} ~0.9 nm (Fig. 3 *A*, *right*). The maximum forces during the unfolding decrease, like in Setup 1, with the pulling speed. The average maximum forces are much lower than for Setup 1 (Table 1). Hence, the only speed dependency is shifting the unbinding event to lower pulling distances and lower forces, without switching the unbinding pathway, despite nearly identical simulation parameters.

Setup 2

Here, we used a different SMD simulation scheme and pulled at the center-of-mass (COM) of the two individual proteins (Fig. 1 *C*). This resulted in drastic changes in the choice of the pathway compared to Setups 1 and 1_m. A different set of specific contacts d_3 to d_5 describes the taken pathways (Fig. 3 *B*).

The main pathway of the COM pulling in Setup 2 was a two-step process. The two-dimensional histogram of the unbinding distances shows that the structural distortion of Barstar at d_3 ~0.9 nm is earlier than the unbinding at d_5 ~1.7 nm (Fig. 3 *B*). First, an internal rearrangement in Barstar moved the core of the protein away from the binding helix, leaving the binding site intact. This increased the separation d_3 until all side-chain interactions of the Barstar binding-helix with the core of the Barstar protein were broken. Second, the Barstar binding helix began to unbind from the binding pocket of Barnase, starting from its C-terminal end. This caused the partial unbinding of the complex, characterized by d_5 (Fig. 3 *B*). For medium and slow pulling, all trajectories unbind (all $d_4 > 0$ nm), whereas, at fast pulling speeds, some trajectories were not fully separated at the end of the simulation. Furthermore, for medium and slow pulling velocities, single trajectories show unbinding of the complex without complex distortions ($d_3 = 0$ nm).

Setup 3

In the third setup, the COM of the C_α-atoms of Barstar's binding helix was pulled (Fig. 1 *D*). This setup was designed to probe the binding site of the Barnase-Barstar complex directly.

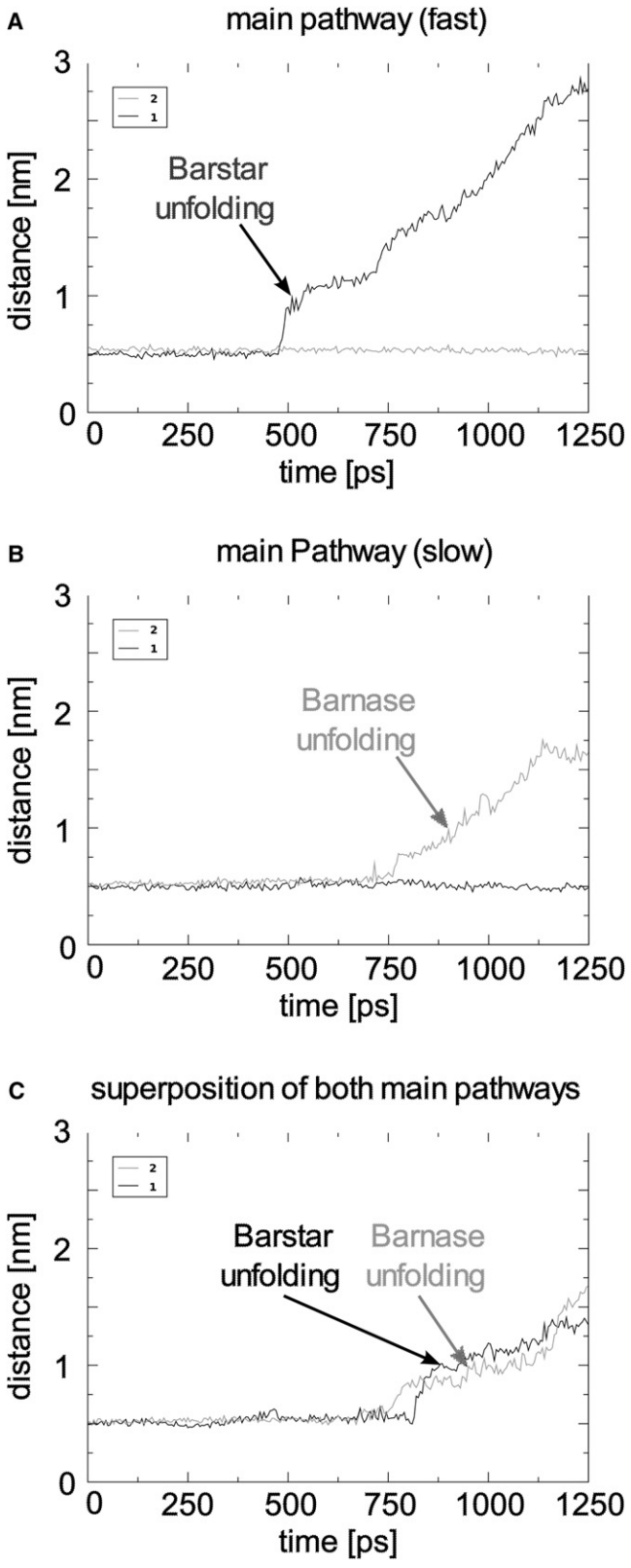

FIGURE 2 Setup 1. These representative distance curves show the development of the unfolding parameters d_1 (*black*) and d_2 (*gray*) representing the three different types of pathways taken during the experiment. The arrows mark the first time at which the contact showed an increased separation of 0.5-nm larger than the equilibrium distance. This time is defined as the separation time t_1 or t_2. The first graph represents the main pathway at fast pulling (*A*), whereas the second shows a typical minor pathway that will become important in the medium pulling (*B*). The third pathway (*C*) can be described as a superposition of the two main pathways (*A* and *B*).

Here, the rupture of the Barnase-Barstar complex was described by a continuous unbinding event. It started at one end of Barstar's binding helix until a fully unbound state was reached. No major distortions in the protein structure of the binding partners were observed.

Unbinding that starts the separation at d_4 or d_5 can be observed. Thus, two unbinding pathways exist. For fast pulling, both pathways are overlapping. For medium pulling, a separation is indicated. For slow pulling, it can be observed in the two populations in the two-dimensional histogram (Fig. 3 *C*).

The main unbinding pathway shifts from starting separation at the C-terminal end of the Barstar binding helix d_5 at high pulling velocities, to starting with an N-terminal separation (d_4) for medium and slow pulling velocities (Fig. 3 *C*).

The forces during the trajectory increase to a maximum force of $\langle F_{\max}\rangle \sim 1.8$ nN. The comparison of the maximum forces depending on the selected pathway show no significant differences (Fig. 4 *B*). The median maximum forces of the major pathway with $\langle F_{\max,\ 5}\rangle = 1.75$ nN is only slightly smaller than $\langle F_{\max,\ 4}\rangle = 1.80$ nN for the minor pathway. The ruptures occurred after the maximum force peak (Fig. 4 *A*). We defined the rupture force in Setup 3 as the force $F(t_{\text{rupt}})$ at the time of the first separation ($t_{\text{rupt}} = \min(t_4, t_5)$). The median of the rupture forces of the major unbinding pathway was $\langle F_5\rangle = 1056$ pN ($t_5 < t_4$) and, surprisingly, higher than of the minor pathway with $\langle F_4\rangle = 786$ pN ($t_5 > t_4$) (Fig. 4 *C*). Since the force describes the slope of the energy landscape, this behavior can be explained with an energy landscape of the unbinding event being an energy funnel with a constantly decreasing slope after the point of the maximum force (Fig. 4 *D*). Hence, the main unbinding pathway has a steeper slope in the energy landscape at the point of breakage.

Viscous drag forces after separation

After the separation of the complex in Setups 2 and 3, the pulling forces exerted on the protein are needed to move the protein through the water. These drag forces F_{drag} were calculated by averaging the forces only after complete separation (Table 3). Additional drag forces during the actual unbinding process are not investigated. Therefore, the drag forces calculated here are only a lower limit of the drag forces during the separation. The total amount of the friction due to viscous drag forces of ~200 pN show that for all pulling velocities, these effects cannot be neglected (Table 3).

A transition from higher to lower drag forces can be seen if the pulling velocity is decreased from fast to medium pulling. No major reduction of the average drag forces can

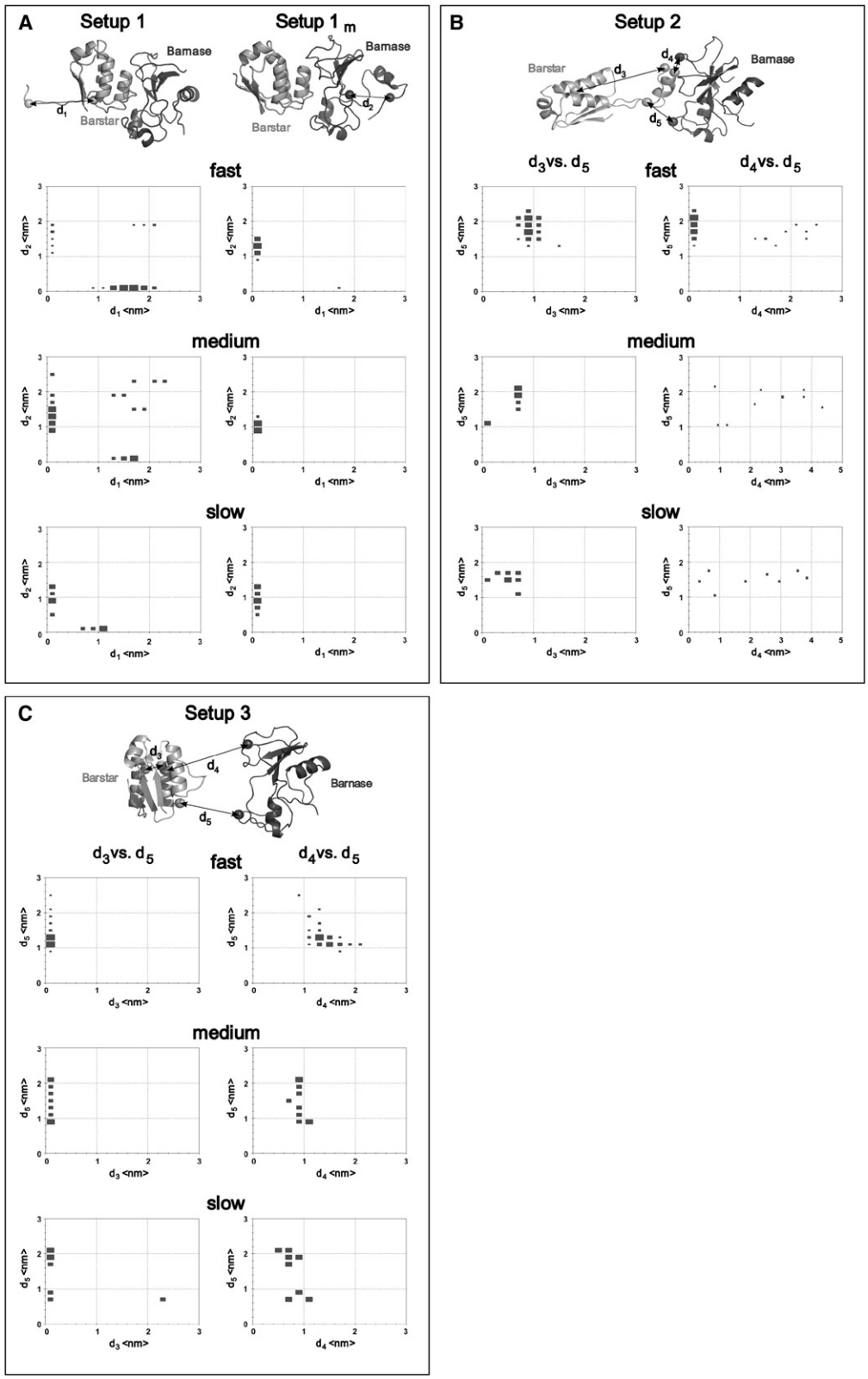

FIGURE 3 The unbinding and unfolding behavior of the Barnase-Barstar complex is shown by a typical snapshot of the unbinding/unfolding structure, as well as by histograms comparing the different pulling distances for the specific contacts d_1–d_5 to rupture. The size of the boxes in the two-dimensional histograms is proportional to the number of events (binning in both directions is 0.2 nm). (*A*) Unfolding of Setups 1 and 1_m. (*B*) Unbinding of Setup 2. (*C*) Unbinding of Setup 3.

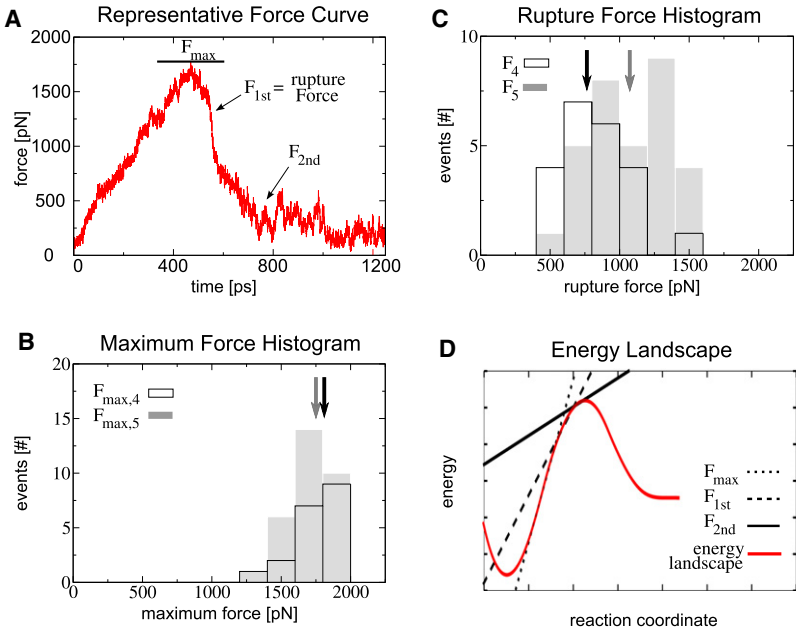

FIGURE 4 Setup 3. (*A*) Representative force time curve of the unbinding event in Setup 3. The maximum force F_{max} occurs earlier than the rupture force (F_{1st}), defined by the force at the time of the first separation. The unbinding ends at a force F_{2nd}, which is in the range of the viscous drag forces after the separation. (*B*) The maximum force histogram shows that major ($F_{max,\ 5}$, *gray bars*) and minor ($F_{max,\ 4}$, *white bars*) pathways are similar. The median maximum forces of the maximum forces are marked as arrows in the histogram. The median of major ($\langle F_{max,\ 5}\rangle = 1.75$ nN, *gray arrow*) and minor ($\langle F_{max,\ 4}\rangle = 1.80$ nN, *black arrow*) pathways were comparable. (*C*) The rupture forces F_5 (*gray bars*) of the main pathway were, on average, higher than the rupture forces F_4 (*white bars*) of the minor pathway. The arrows, denoting the median rupture forces of the major ($\langle F_5\rangle = 1056$ pN, *gray arrow*) and minor ($\langle F_{max,\ 5}\rangle = 786$ nN, *black arrow*) pathways, show that for the major pathway higher forces were needed. (*D*) The continuous unbinding process can be described with a funnel-shaped energy landscape. With increased reaction coordinate, the forces, represented by the slope of the energy profile at a given reaction coordinate, diminish after F_{max} was reached.

be detected when decreasing the pulling velocity from medium to slow speeds. In contrast to this, the average of the maximum pulling forces for Setups 2 and 3 decrease with every pulling velocity reduction (Table 1). The higher viscous drag forces of Setup 2 compared with Setup 3 during fast pulling can be attributed to the increased surface area of the Barstar in Setup 2 due to the extended protein distortions. However, even though the viscous drag forces are higher in Setup 2, Setup 3 shows the higher average maximum forces.

Effective work of the protein-protein separation

For Setups 2 and 3, the average effective work $\langle W_{eff}(x)\rangle$ on the protein complex depending on the reaction coordinate x (distance pulled) was calculated (Fig. 5, *A* and *B*). For both setups, lower pulling velocities result in lower work due to increased sampling of the energy landscape perpendicular to the reaction coordinate.

The comparison of Setups 2 and 3 shows that the final effective work of separation is comparable (Fig. 5, *C–E*). The work in Setup 2 is higher due to additional conformational distortions during the separation of the complex. To separate Barnase and Barstar, Setup 2 requires ~1 nm additional pulling distance, which leads to an increase in simulation time of ~66% compared to Setup 3.

TABLE 3 The calculated drag forces of the pulled molecules through water after the complete separation of the protein complex

	$\langle F_{drag}\rangle$/pN	stdDev($\langle F_{drag}\rangle$)/pN	No. of separations	No. of trajectories
Setup 2				
Fast	253	25	9	67
Medium	178	10	10	10
Slow	176	22	8	8
Setup 3				
Fast	207	20	55	55
Medium	173	7	10	10
Slow	171	5	8	8

DISCUSSION

Free, thermal, and forced unfolding

Free, thermal, and chemical unfolding are different from enforced unfolding (1,10,60). The spontaneous unfolding of Barnase, without the complexing Barstar, was shown to differ from the forced unfolding by the import machinery of the Mitochondria. The spontaneous unfolding starts at the center region of the protein; the forced unfolding starts at the N-terminal end without previously inducing a molten globule state at the import site (1,10), while thermal unfolding induced structural changes within the protein's core (11). These results are in line with our simulations in Setup 1 and Setup 1_m, where for slower pulling we also observe an unfolding starting from the N-terminus of Barstar independent of the force vector.

Barnase-Barstar in comparison to other proteins

AFM experiments on a fusion protein consisting of a Barnase domain fused to titin I27 domains showed that Barnase unfolds at lower forces than the titin domain. The chimera was pulled at the terminal ends of the proteins (11), leading to force vectors analogous to our Setup 1. To compare these experimental results with our simulation, we extrapolated the titin unfolding forces observed in previous simulations to the loading rates of our simulations. All forces were extrapolated due to their logarithmic dependency on the loading rate (9,61),

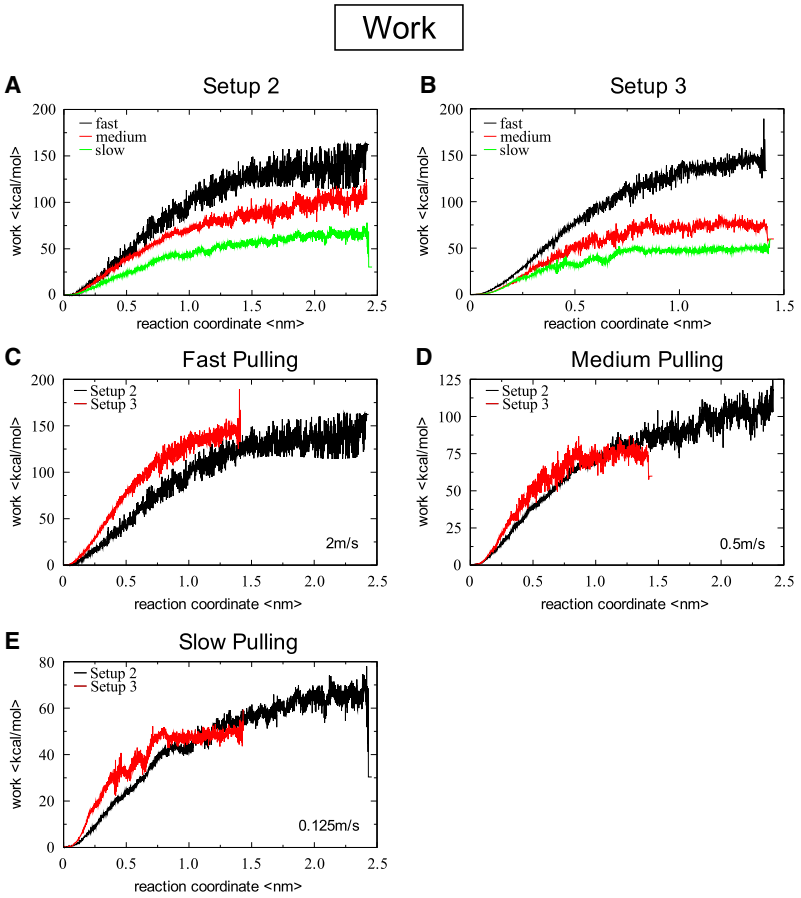

FIGURE 5 The effective work versus the pulled distance as reaction coordinate for Setup 2 (*A*) and Setup 3 (*B*) is shown. The work decreases with decreasing pulling velocity from fast pulling at 2 m/s (highest work curve), over medium pulling at 0.5 m/s (middle work curve), to slow pulling at 0.125 m/s (lowest work curve). The separation of the Barnase-Barstar complex is reached at comparable average effective work values for both setups, but for a separation in Setup 2 one needs ~1 nm additional pulling compared to Setup 3. The direct comparison of the work in Setup 2 and 3 for fast (*C*), medium (*D*), and slow (*E*) pulling is also shown. (Setup 2 ranges from 0–~2.5nm; Setup 3 from 0–~1.5nm).

$$F_{\text{rupt}} = \frac{k_{\text{B}}T}{\Delta x} \times ln\left(\frac{\upsilon \times \Delta x}{k^0_{\text{off}} \times k_{\text{B}}T}\right), \quad (3)$$

with the loading rate υ, the potential width of the bond Δx, the Boltzmann constant k_{B}, the temperature T, and the natural off-rate $k^0{}_{\text{off}}$. This leads to

$$F_{\text{rupt}}(\upsilon_1) - F_{\text{rupt}}(\upsilon_2) = \alpha \times \ln\left(\frac{\upsilon_1}{\upsilon_2}\right) \quad (4)$$

and results in an extrapolation formula for the rupture force of

$$F_{\text{extr}}(\upsilon) = \alpha \times \ln\frac{\upsilon}{\upsilon_1} + F_{\text{rupt}}(\upsilon_1) \quad (5)$$

with

$$\alpha = \frac{k_{\text{B}}T}{\Delta x} = \frac{F_{\text{rupt}}(\upsilon_1) - F_{\text{rupt}}(\upsilon_2)}{\ln\left(\frac{\upsilon_1}{\upsilon_2}\right)}, \quad (6)$$

where two data points (υ_{i}, $F_{\text{rupt}}(\upsilon_{\text{i}})$) need to be known. The loading rates in Eqs. 5 and 6 are dimensionless.

In agreement with experiment, the average maximum forces of the Barnase unfolding in Setup 1 (951 pN) and Setup 1_{m} (828 pN) are lower than the extrapolated unfolding forces of the titin domain I27 of 1228 pN (Table 4) (62). Also the unfolding forces of titin domain I1 in its oxidized ($F_{\text{extr}} = 1171$ pN) as well as its reduced form ($F_{\text{extr}} = 1022$ pN) are higher (Table 4). The pull-and-wait pulling protocol by Pabón and Amzel produced an even higher Force peak of 1440 pN (63). Since only one loading rate pair is known, this force was not extrapolated. The energy for the unfolding of the force-transmitting domain I27 of titin ($500\frac{\text{kcal}}{\text{mol}}$) (64) is much higher than for the unbinding of the Barnase-Barstar system ($< 150\frac{\text{kcal}}{\text{mol}}$ in Table 5). These data demonstrate the mechanical instability of the Barnase-Barstar system as opposed to the titin family, a family that is designed to operate in a force-exerting environment.

The extrapolated unbinding forces of reported data on Barnase unfolding (11) are comparable to our unbinding forces within the error, if not higher (Table 4). This indicates that due to the N-terminal unfolding of Barnase, the protein is not significantly stabilized by being complexed with Barstar.

Antibody-antigen interactions, where the antigen is a small helical peptide, showed lower unbinding forces compared to our results of Setups 2 and 3, but comparable forces to our unfolding forces (Tables 1 and 4). This demonstrates 1), the high affinity of the Barnase-Barstar complex; and 2), the low mechanical stability of the complex.

The rupture forces observed for the TCR-pMHC complex and cytochrome *c*2 exceed the forces observed in our simulations (Table 4) (35,37).

TABLE 4 The unfolding/unbinding forces and loading rates of a variety of simulated and experimental data

System (reference)	Reference	Attachment	Force/pN	Loading rate/ $\frac{pN}{ns}$	Extrapolated force/pN
Experimental unfolding					
Barnase AFM	(11)		100	2.1×10^{-6}	
Barstar AFM	(65)		<50		
Simulated unfolding					
Barnase	(11)	C-C	507	1390	968
Barnase	(11)	C-C	269	695	968
Barstar	(65)	C-C	625		
Titin kinase activation	(32)	C-C(2springs)	500	332	988
Titin kinase activation	(32)	C-C(2springs)	1350	41500	988
Titin I27	(62)		2479	145000	1228
Titin I27	(62)		1870	29000	1228
Titin I27	(63)	Pull-and-wait	1440		
Titin I1 oxidized	(62)		2397	145000	1171
Titin I1 oxidized	(62)		1800	29000	1171
Titin I1 reduced	(62)		2090	145000	1022
Titin I1 reduced	(62)		1570	29000	1022
Ubiquitin	(26)	N-Term-C-Term	2000	41420	
Ubiquitin	(26)	Lys48-C-Term	1200	41420	
Simulated deformation					
α-Helix stretching			500		
β-Sheet longitudinal shear	(23)		1000		
β-Sheet lateral shear	(23)		40–120		
α-Helix longitudinal shear	(23)		65–150		
α-Helix lateral shear	(23)		200		
Simulated unbinding in literature					
TCR-pMHC	(37)	Individual	1660		
Streptavidin-biotin	(70)		800		
Antibody-antigen	(36)	C(N-Term)-COM	716	6640	
Antibody-antigen	(36)	C(Middle)-COM	1161	6640	
Antibody-antigen	(36)	C(C-Term)-COM	775	6640	
Cytochrome *c*2	(35)	Absolute COM	1500	6943.5	

Extrapolated force peak values at the loading rate of our fast pulling experiments ($v = 5320\frac{pN}{ns}$) were estimated according to Eq. 5. Two data points at different loading rates were used for the extrapolation.

In a biological context, the mechanical instability contrasts the equilibrium affinity of the complex. Under equilibrium conditions, the complex has an extremely low off-rate and virtually never unbinds. The equilibrium stability of the complex poses some conceptual problems: while within the cell, Barnase certainly needs to be complexed to ensure cell survival, and the complex somehow must be opened to export Barnase. The mechanical instability may be needed to unfold the complex during export of Barnase to the extracellular space, which would allow the inhibitor to unbind only at the point of export, and which is consistent with the N-terminal position of the signal peptide. This would pose an interesting balance between different aspects of mechanical-versus-equilibrium stability, which would ensure maximum protection of the cell while allowing for unbinding during export.

Influence of drag force

For fast probing, the complex is unfolding at different ends of the complex (Fig. 3 *A*) in Setups 1 and 1_m. Since all other parameters are identical, the reason for this different behavior is the opposite direction of the probing force vector. The pulling force F_{pull} is compensated by the harmonic potential holding the protein (F_{hold}) and the opposing pressure of the solvent F_{solv} (viscous drag). The harmonic potentials (F_{pull} and F_{hold}) are invariant to the pulling direction. Therefore, in the absence of solvent, one would not expect differences between Setups 1 and 1_m. However, the solvent causes a strongly direction-dependent drag force, which is also sensitive to the attachment point of the force.

Due to the viscous drag, $F_{pull} > F_{hold}$ under nonequilibrium conditions. Therefore, in Setup 1, $F_{bs} > F_{bn}$ and in Setup 1_m, $F_{bn} > F_{bs}$. These differences in force caused by drag can explain the observed differences in the trajectories at high loading rates. At lower loading rates, the influence of the drag force is reduced (Table 3), rendering the simulations more similar (Fig. 3). For dual unfolding at both ends, two barriers need to be overcome, reducing the probability of such events.

Distortions in Setups 1 and 1_m

At fast loading rates, due to the unfolding of Barstar's final β-sheet, the structural core of the protein gets disturbed in Setup 1. The concerted motion of the helix away from the

TABLE 5 Computed energies of the Barnase-Barstar and comparable energies found in literature

System	Reference	Energy or work/ $\frac{kcal}{mol}$
Experimental unfolding		ΔG
Barstar free energy of unfolding ΔG	(43)	−5.28
Barnase unfolding stability ΔG	(11)	10.2
Simulated unfolding		ΔW
Titin I27 total interaction energy ΔW[	(64)	500
Simulated deformation energies		ΔE
ΔE of secondary structure elements		
α-Helix stretching	(23)	50
β-Sheet longitudinal shear	(23)	40
β-Sheet lateral shear	(23)	40
α-Helix longitudinal shear	(23)	20
α-Helix lateral shear	(23)	20
Experimental binding energy		ΔG
Barnase-Barstar free energy of binding ΔG	(39)	−19
Simulated unbinding		Work ΔW
Barnase-Barstar Setup 2—fast		147
Barnase-Barstar Setup 3—fast		144
Barnase-Barstar Setup 2—medium		106
Barnase-Barstar Setup 3—medium		71
Barnase-Barstar Setup 2—slow		56
Barnase-Barstar Setup 3—slow		51
TCR-pMHC unbinding	(37)	380

structural core of Barnase, in contrast, leaves all the secondary structure elements intact. Only a few contacts between helix and structural core are broken (Fig. 6). The lateral unbinding of the N-terminal helix of Barnase is a gradual, zipperlike process, while the unfolding of the Barstar β-sheet is a catastrophic, cooperative event (Fig. 6). The shearing of a β-sheet has been implicated to be energetically more costly: it has been shown that the lateral shearing of helix pairs (comparable to the shearing away of Barnase's helix observed here) is energetically more favorable than the shearing of β-sheets (Tables 4 and 5) (23). Furthermore, Gräter et al. showed that the probed geometry of β-sheets is very stable (32). Our observations at slow pulling velocities, where the system has more time to relax orthogonally to the pulling vector and where the unfolding of the Barstar β-sheet is not observed, support this notion. At slower pulling velocities, only the shearing of the helix is observed, being the thermodynamically more favorable process. AFM experiments as well as theoretical considerations showed the mechanical lability of Barnase and Barstar (11,60,65) (Tables 4 and 5), in line with the unfolding observed here. In particular, Barnase was suggested to unfold during mitochondrial import at forces as low as ~10 pN (60). Hence, the unfolding of Barnase does not seem to be an artifact of the pulling velocities employed.

Distortions in Setups 2 and 3

To avoid unfolding in the simulations and to gain approximate insight into equilibrium barriers, different simulation schemes need to be employed (37). One possibility would be to go to significantly lower velocities approaching adiabatic conditions, which is hampered by the accompanied computational cost. Recently, Cuendet and Michielin developed an attractive simulation scheme, where the steering force acts only in the direction of the reaction coordinate (37). For the sake of simplicity, we changed the attachment of the probing force and pulled at the centers-of-mass of different groups of the complex. Unbinding simulations of complexes often used larger pulling/attachment groups for avoiding unfolding (35–37).

Attaching the pulling and holding forces to the COM of the molecules distributed the applied tension equally over the whole molecules (Setup 2). Although these simulations are not easily reproduced by AFM measurements, they nevertheless can give insight into aspects of the complex observable by other techniques like double mutant cycle or folding measurements. The resulting structural distortions of the Barstar show that the overall structural integrity of Barstar is weaker than that of Barnase, as also shown experimentally (Table 5).

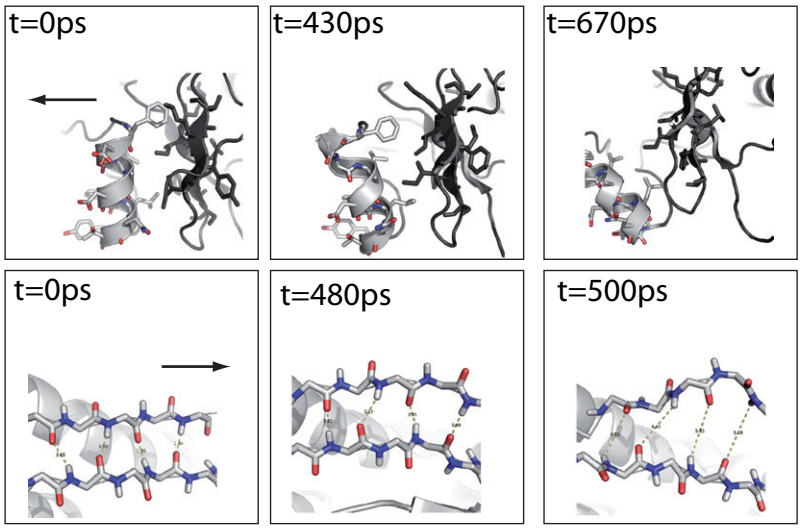

FIGURE 6 The unfolding trajectories of Setups 1 and 1_m are shown. (*Upper panel*) Shearing of Barnase helix. (*Lower panel*) Shearing of Barstar sheet. The arrows indicate the direction of the force vector.

We probe here the stability of the binding of this helix to Barnase, relative to the binding strength to its own protein core in a differential force assay. Since the here-probed off-rate of the complex is dominated by van der Waals interactions, our results demonstrate that these interactions of Barstar's binding helix with its own protein core are weaker than the interaction with the active side of the RNase Barnase. In an evolutionary point of view, the blocking of the active site of the Barnase is essential to prevent damage to its parental bacterium, while the interaction of Barstar's binding helix with its own protein core is only necessary for the orientation of its charges in the association process (66,67). These charges destabilized Barstar additionally, facilitating the unfolding of the inhibitor (43), in agreement with our results. For even lower pulling velocities than used here, the distortions will probably not be observed, as indicated by rare events at slow pulling velocities.

Directly addressing the pulling forces to Barstar's binding helix (Setup 3) results in unbinding without structural distortions. The stiffness of the helix (23) distributes the external mechanical tension over the binding interface. The majority of all direct Barnase-Barstar interactions are mediated by this helix.

Unbinding pathways

In Setup 3, unbinding pathways without structural distortions are observed. The high maximum forces (Table 1) point to a very strong binding of the inhibitor to its RNase. A closer examination of the complex unbinding reveals that the main unbinding pathway started separating the complex from the C-terminal end of Barstar's binding helix for fast pulling, and from the N-terminal for medium and slow pulling (Fig. 3 *C*, *right*).

For both pathways, the last contacts involve $Arg_{bn}59$, $Asp_{bs}35$, and $Asp_{bs}39$ (Fig. 7). These residues have been implicated to be important for the association pathway of the complex under equilibrium conditions, in particular the loop from residue 57 to residue 60 of Barnase (41,48). This indicates that the observed, enforced dissociation pathways are a good approximation of equilibrium association pathways. Based on Brownian dynamics simulations, the overlap of association and dissociation pathways has been suggested before (51). The agreement of our simulated dissociation pathway with proposed association pathways shows that the probing of the central helix allows us to sample essential barriers of the equilibrium trajectory. Even the effective work of enforced unbinding, with $W_{\mathrm{eff}}^{\mathrm{Setup3}} = 51\frac{\mathrm{kcalc}}{\mathrm{mol}}$, is only

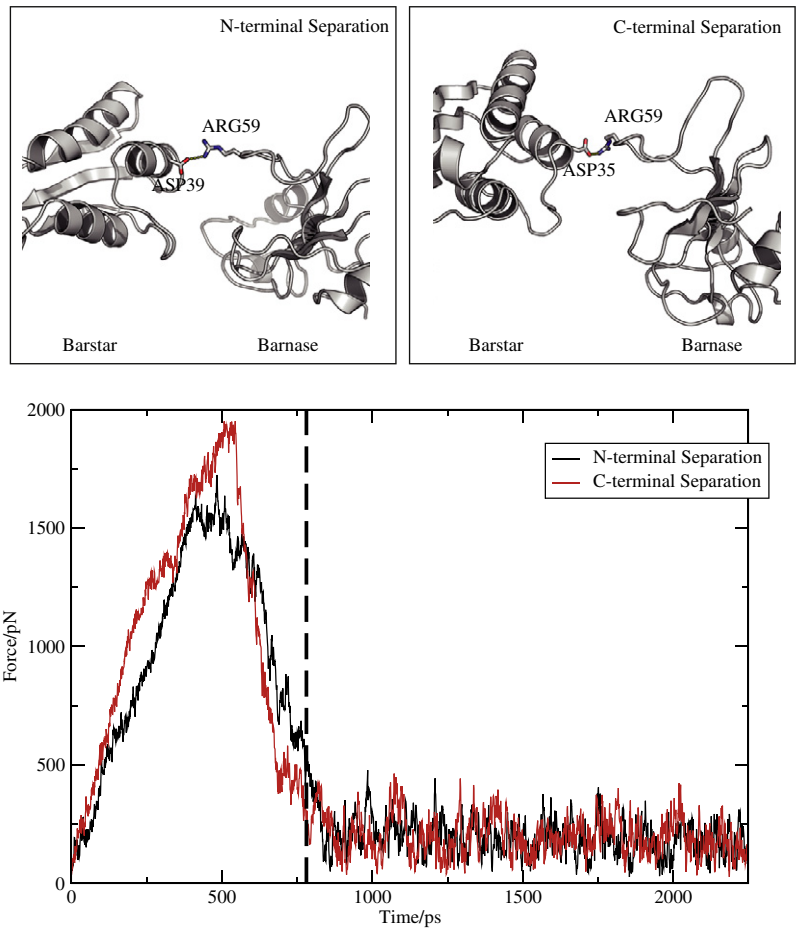

FIGURE 7 Typical last contacts for Setup 3 (*upper panel*) and the time of separation (*dashed line* in *lower panel*) of these last contacts in the force distance trace are shown.

2–3 times the experimentally determined binding energy of the complex of $\delta G_{\mathrm{ass}} = -19\frac{\mathrm{kcalc}}{\mathrm{mol}}$ (39) (Table 5), being thus in a comparable range despite the nonequilibrium nature of our simulations. More complex nonequilibrium simulation schemes of a large protein-protein complex did not reach a better agreement (37). The effective work values of Setups 2 and 3 show that the conformational distortions in Setup 2 require additional work, especially for the faster and medium pulling velocities (Table 5).

We did not attempt to use nonequilibrium analysis schemes like the Jarzynski relation (68). These relations depend on the observation of rare events. The probability of these events becomes negligible with increasing dissipation and system size (69). Standard evaluation schemes use the cumulative expansion of the Jarzynski relation, which is dependent on a Gaussian distribution of work values (69). A Gaussian distribution is not usually observed in simulations with a limited number of trajectories (37).

CONCLUSION

The velocity and geometry of the force application have a strong effect on the evolution of a system. Rapidly changing a system may probe the lability of the energy landscape. This may be very different from slow changes, which test the stability of the system. Furthermore, the different attachment points of force have a severe influence on the final conformation. Summarizing, we showed that an atomistic understanding of unbinding or unfolding pathways needs the application of a variety of force protocols. The applied forces alter the energy landscape in a nontrivial way. The resulting propagation of the probed protein through phase space does not only critically depend on the geometry of force application, but equally on the velocity of force application. Therefore, for a thorough characterization of the effect of force on a protein complex, multiple simulations with different probing geometries and different velocities need to be performed, carefully testing the lability and stability of the system. Sophisticated attachment simulation schemes allow rapid, but approximate insight into the main barriers of the dissociation pathways, deepening our understanding of the observed system and helping in the design of experiments.

We thank R. D. Astumian and M. Höfling for helpful discussions.

Financial support from the Fonds der Chemischen Industrie, the Center for NanoScience, and the International Doctorate Program Nano-Bio-Technology of the Elitenetzwerk Bayern is acknowledged.

REFERENCES

1. Huang, S., S. Murphy, and A. Matouschek. 2000. Effect of the protein import machinery at the mitochondrial surface on precursor stability. *Proc. Natl. Acad. Sci. USA*. 97:12991–12996.
2. Sukharev, M., Betanzos, C. S. Chiang, and H. Guy. 2001. The gating mechanism of the large mechanosensitive channel MscL. *Nature*. 409:720–724.
3. Bershadsky, A. D., N. Q. Balaban, and B. Geiger. 2003. Adhesion-dependent cell mechanosensitivity. *Annu. Rev. Cell Dev. Biol.* 19:677–695.
4. Evans, E., A. Leung, V. Heinrich, and C. Zhu. 2004. Mechanical switching and coupling between two dissociation pathways in a P-selectin adhesion bond. *Proc. Natl. Acad. Sci. USA*. 101:11281–11286.
5. Gumbart, J., M. C. Wiener, and E. Tajkhorshid. 2007. Mechanics of force propagation in TonB-dependent outer membrane transport. *Biophys. J.* 93:496–504.
6. Nevo, R., V. Brumfeld, R. Kapon, P. Hinterdorfer, and Z. Reich. 2005. Direct measurement of protein energy landscape roughness. *EMBO Rep.* 6:482–486.
7. Barsegov, V., and D. Thirumalai. 2005. Probing protein-protein interactions by dynamic force correlation spectroscopy. *Phys. Rev. Lett.* 95:168302.
8. Kessler, M., K. E. Gottschalk, H. Janovjak, D. J. Muller, and H. E. Gaub. 2006. Bacteriorhodopsin folds into the membrane against an external force. *J. Mol. Biol.* 357:644–654.
9. Evans, E., and K. Ritchie. 1997. Dynamic strength of molecular adhesion bonds. *Biophys. J.* 72:1541–1555.
10. Huang, S., K. S. Ratliff, M. P. Schwartz, J. M. Spenner, and A. Matouschek. 1999. Mitochondria unfold precursor proteins by unraveling them from their N-termini. *Nat. Struct. Biol.* 6:1132–1138.
11. Best, R. B., B. Li, A. Steward, V. Daggett, and J. Clarke. 2001. Can non-mechanical proteins withstand force? Stretching Barnase by atomic force microscopy and molecular dynamics simulation. *Biophys. J.* 81:2344–2356.
12. Evans, E., K. Ritchie, and R. Merkel. 1995. Sensitive force technique to probe molecular adhesion and structural linkages at biological interfaces. *Biophys. J.* 68:2580–2587.
13. Grubmüller, H., B. Heymann, and P. Tavan. 1996. Ligand binding: molecular mechanics calculation of the streptavidin-biotin rupture force. *Science*. 271:997–999.
14. Rief, M., M. Gautel, F. Oesterhelt, J. M. Fernandez, and H. E. Gaub. 1997. Reversible unfolding of individual titin immunoglobulin domains by AFM. *Science*. 276:1109–1112.
15. Lu, H., and K. Schulten. 1999. Steered molecular dynamics simulations of force-induced protein domain unfolding. *Proteins*. 35:453–463.
16. Oesterhelt, F., D. Oesterhelt, M. Pfeiffer, A. Engel, H. E. Gaub, et al. 2000. Unfolding pathways of individual bacteriorhodopsins. *Science*. 288:143–146.
17. Gao, M., D. Craig, V. Vogel, and K. Schulten. 2002. Identifying unfolding intermediates of FN-III(10) by steered molecular dynamics. *J. Mol. Biol.* 323:939–950.
18. Grubmüller, H. 2005. Force probe molecular dynamics simulations. *Methods Mol. Biol.* 305:493–515.
19. Gao, S., M. Sotomayor, E. Villa, E. H. Lee, and K. Schulten. 2006. Molecular mechanisms of cellular mechanics. *Phys. Chem. Chem. Phys.* 8:3692–3706.
20. Kessler, M., and H. E. Gaub. 2006. Unfolding barriers in bacteriorhodopsin probed from the cytoplasmic and the extracellular side by AFM. *Structure*. 14:521–527.
21. Vogel, V. 2006. Mechanotransduction involving multimodular proteins: converting force into biochemical signals. *Annu. Rev. Biophys. Biomol. Struct.* 35:459–488.
22. Sotomayor, M., and K. Schulten. 2007. Single-molecule experiments in vitro and in silico. *Science*. 316:1144–1148.
23. Rohs, R., C. Etchebest, and R. Lavery. 1999. Unraveling proteins: a molecular mechanics study. *Biophys. J.* 76:2760–2768.
24. Bryant, Z., V. S. Pande, and D. S. Rokhsar. 2000. Mechanical unfolding of a β-hairpin using molecular dynamics. *Biophys. J.* 78:584–589.
25. Brockwell, D. J., E. Paci, R. C. Zinober, G. S. Beddard, P. D. Olmsted, et al. 2003. Pulling geometry defines the mechanical resistance of a β-sheet protein. *Nat. Struct. Biol.* 10:731–737.

26. Carrion-Vazquez, M., H. Li, H. Lu, P. E. Marszalek, A. F. Oberhauser, et al. 2003. The mechanical stability of ubiquitin is linkage dependent. *Nat. Struct. Biol.* 10:738–743.
27. Li, P.-C., and D. E. Makarov. 2004. Simulation of the mechanical unfolding of ubiquitin: probing different unfolding reaction coordinates by changing the pulling geometry. *J. Chem. Phys.* 121:4826–4832.
28. Eyal, E., and I. Bahar. 2008. Toward a molecular understanding of the anisotropic response of proteins to external forces: insights from elastic network models. *Biophys. J.* 94:3424–3435.
29. Gee, E. P. S., D. E. Ingber, and C. M. Stultz. 2008. Fibronectin unfolding revisited: modeling cell traction-mediated unfolding of the tenth type-III repeat. *PLoS ONE.* 3:e2373.
30. Dietz, H., and M. Rief. 2004. Exploring the energy landscape of GFP by single-molecule mechanical experiments. *Proc. Natl. Acad. Sci. USA.* 101:16192–161971.
31. Dietz, H., and M. Rief. 2008. Elastic bond network model for protein unfolding mechanics. *Phys. Rev. Lett.* 100:098101.
32. Gräter, F., J. H. Shen, H. L. Jiang, M. Gautel, and H. Grubmüller. 2005. Mechanically induced titin kinase activation studied by force-probe molecular dynamics simulations. *Biophys. J.* 88:790–804.
33. Puchner, E. M., A. Alexandrovich, A. L. Kho, U. Hensen, L. V. Schäfer, et al. 2008. Mechanoenzymatics of titin kinase. *Proc. Natl. Acad. Sci. USA.* 105:13385–13390.
34. Gräter, F., and H. Grubmüller. 2007. Fluctuations of primary ubiquitin folding intermediates in a force clamp. *J. Struct. Biol.* 157:557–569.
35. Autenrieth, F., E. Tajkhorshid, K. Schulten, and Z. Luthey-Schulten. 2004. Role of water in transient cytochrome *c*2 docking. *J. Phys. Chem. B.* 108:20376–20387.
36. Morfill, J., J. Neumann, K. Blank, U. Steinbach, E. M. Puchner, et al. 2008. Force-based analysis of multidimensional energy landscapes: application of dynamic force spectroscopy and steered molecular dynamics simulations to an antibody fragment-peptide complex. *J. Mol. Biol.* 381:1253–1266.
37. Cuendet, M. A., and O. Michielin. 2008. Protein-protein interaction investigated by steered molecular dynamics: the TCR-pMHC complex. *Biophys. J.* 95:3575–3590.
38. Hartley, R. W. 1989. Barnase and Barstar: two small proteins to fold and fit together. *Trends Biochem. Sci.* 14:450–454.
39. Schreiber, G., and A. R. Fersht. 1995. Energetics of protein-protein interactions: analysis of the Barnase-Barstar interface by single mutations and double mutant cycles. *J. Mol. Biol.* 248:478–486.
40. Schreiber, G., C. Frisch, and A. R. Fersht. 1997. The role of Glu-73 of Barnase in catalysis and the binding of Barstar. *J. Mol. Biol.* 270:111–122.
41. Frisch, C., A. R. Fersht, and G. Schreiber. 2001. Experimental assignment of the structure of the transition state for the association of Barnase and Barstar. *J. Mol. Biol.* 308:69–77.
42. Matouschek, A. 2003. Protein unfolding—an important process in vivo? *Curr. Opin. Struct. Biol.* 13:98–109.
43. Schreiber, G., A. M. Buckle, and A. R. Fersht. 1994. Stability and function: two constraints in the evolution of Barstar and other proteins. *Structure.* 2:945–951.
44. Schreiber, G., and A. R. Fersht. 1996. Rapid, electrostatically assisted association of proteins. *Nat. Struct. Biol.* 3:427–431.
45. Vijayakumar, M., K. Y. Wong, G. Schreiber, A. R. Fersht, A. Szabo, et al. 1998. Electrostatic enhancement of diffusion-controlled protein-protein association: comparison of theory and experiment on Barnase and Barstar. *J. Mol. Biol.* 278:1015–1024.
46. Schreiber, G., Y. Shaul, and K. E. Gottschalk. 2006. Electrostatic design of protein-protein association rates. *Methods Mol. Biol.* 340:235–249.
47. Dong, F., M. Vijayakumar, and H.-X. Zhou. 2003. Comparison of calculation and experiment implicates significant electrostatic contributions to the binding stability of Barnase and Barstar. *Biophys. J.* 85:49–60.
48. Gabdoulline, R. R., and R. C. Wade. 1997. Simulation of the diffusional association of Barnase and Barstar. *Biophys. J.* 72:1917–1929.
49. Gabdoulline, R. R., and R. C. Wade. 2001. Protein-protein association: investigation of factors influencing association rates by Brownian dynamics simulations. *J. Mol. Biol.* 306:1139–1155.
50. Camacho, C. J., Z. Weng, S. Vajda, and C. DeLisi. 1999. Free energy landscapes of encounter complexes in protein-protein association. *Biophys. J.* 76:1166–1178.
51. Spaar, A., C. Dammer, R. R. Gabdoulline, R. C. Wade, and V. Helms. 2006. Diffusional encounter of Barnase and Barstar. *Biophys. J.* 90:1913–1924.
52. Buckle, A. M., G. Schreiber, and A. R. Fersht. 1994. Protein-protein recognition: crystal structural analysis of a Barnase-Barstar complex at 2.0-Å resolution. *Biochemistry.* 33:8878–8889.
53. Lindahl, E., B. Hess, and D. van der Spoel. 2001. GROMACS 3.0: a package for molecular simulation and trajectory analysis. *J. Mol. Model.* 7:306–317.
54. van der Spoel, D., E. Lindahl, B. Hess, G. Groenhof, A. E. Mark, et al. 2005. GROMACS: fast, flexible, and free. *J. Comput. Chem.* 26:1701–1718.
55. Berendsen, H. J. C., J. R. Grigera, and T. P. Straatsma. 1987. The missing term in effective pair potentials. *J. Phys. Chem.* 91:6269–6271.
56. Jorgensen, W. L., D. S. Maxwell, and J. Tirado-Rives. 1996. Development and testing of the OplS all-atom force field on conformational energetics and properties of organic liquids. *J. Am. Chem. Soc.* 118:11225–11236.
57. Hess, B., H. Bekker, H. J. C. Berendsen, and J. G. E. M. Fraaije. 1997. LINCS: a linear constraint solver for molecular simulations. *J. Comp. Chem.* 18:1463–1472.
58. Berendsen, H., J. Postma, W. van Gunsteren, A. Dinola, and J. Haak. 1984. Molecular dynamics with coupling to an external bath. *J. Chem. Phys.* 81:3684–3690.
59. Ewald, P. P. 1921. Die Berechnung optischer und elektrostatischer Gitterpotentiale. *Ann. Phys.* 64:253–287.
60. Shariff, K., S. Ghosal, and A. Matouschek. 2004. The force exerted by the membrane potential during protein import into the mitochondrial matrix. *Biophys. J.* 86:3647–3652.
61. Friedsam, C., A. K. Wiehle, F. Kuhner, and H. E. Gaub. 2003. Dynamic single-molecule force spectroscopy: bond rupture analysis with variable spacer length. *J. Phys. Cond. Mat.* 15:S1709–S1723.
62. Gao, M., M. Wilmanns, and K. Schulten. 2002. Steered molecular dynamics studies of titin I1 domain unfolding. *Biophys. J.* 83:3435–3445.
63. Pabón, G., and L. M. Amzel. 2006. Mechanism of titin unfolding by force: insight from quasi-equilibrium molecular dynamics calculations. *Biophys. J.* 91:467–472.
64. Lu, H., B. Isralewitz, A. Krammer, V. Vogel, and K. Schulten. 1998. Unfolding of titin immunoglobulin domains by steered molecular dynamics simulation. *Biophys. J.* 75:662–671.
65. Sharma, D., G. Feng, D. Khor, G. Z. Genchev, H. Lu, et al. 2008. Stabilization provided by neighboring strands is critical for the mechanical stability of proteins. *Biophys. J.* 95:3935–3942.
66. Selzer, T., and G. Schreiber. 1999. Predicting the rate enhancement of protein complex formation from the electrostatic energy of interaction. *J. Mol. Biol.* 287:409–419.
67. Selzer, T., S. Albeck, and G. Schreiber. 2000. Rational design of faster associating and tighter binding protein complexes. *Nat. Struct. Biol.* 7:537–541.
68. Chernyak, V., M. Chertkov, and C. Jarzynski. 2005. Dynamical generalization of nonequilibrium work relation. *Phys. Rev. E Stat. Nonlin. Soft Matter Phys.* 71:025102.
69. Park, S., and K. Schulten. 2004. Calculating potentials of mean force from steered molecular dynamics simulations. *J. Chem. Phys.* 120: 5946–5961.
70. Izrailev, S., S. Stepaniants, M. Balsera, Y. Oono, and K. Schulten. 1997. Molecular dynamics study of unbinding of the avidin-biotin complex. *Biophys. J.* 72:1568–1581.